



Probing the role of nickel dopant in aqueous colloidal ZnS nanocrystals for efficient solar-driven CO₂ reduction

Hong Pang^{a,b}, Xianguang Meng^{b,c,*}, Hui Song^{a,b}, Wei Zhou^d, Gaoliang Yang^{a,b}, Hongwei Zhang^e, Yasuo Izumi^e, Toshiaki Takei^b, Wipakorn Jewasuwat^b, Naoki Fukata^b, Jinhua Ye^{a,b,f,g,*}

^a Graduate School of Chemical Science and Engineering, Hokkaido University, Sapporo, 060-0814, Japan

^b International Center for Materials Nanoarchitectonics (WPI-MANA), National Institute for Materials Science (NIMS), Namiki 1-1, Tsukuba, Ibaraki, 305-0044, Japan

^c Hebei Provincial Key Laboratory of Inorganic Nonmetallic Materials, College of Materials Science and Engineering, North China University of Science and Technology, Tangshan, 063210, PR China

^d Department of Applied Physics, Tianjin Key Laboratory of Low Dimensional Materials Physics, Preparing Technology Faculty of Science, Tianjin University, Tianjin, 300072, PR China

^e Department of Chemistry, Graduate School of Science, Chiba University, Yayoi 1-33, Inage-ku, Chiba, 263-8522, Japan

^f TJU-NIMS International Collaboration Laboratory, School of Materials Science and Engineering, Tianjin University, Tianjin, 300072, PR China

^g Collaborative Innovation Center of Chemical Science and Engineering (Tianjin), Tianjin, 300072, PR China

ARTICLE INFO

Keywords:

Photocatalysis
CO₂ reduction
ZnS
Doping
Vacancy

ABSTRACT

Photocatalytic CO₂ reduction reaction (CO₂RR) on a heterogeneous catalyst offers the possibility for CO₂ abatement and emerges as a promising avenue for renewable carbonaceous fuels production at ambient temperature and pressure using solar light as the sole energy input. Here, we report a newly aqueous colloidal comprised of monodispersed Ni-doped ZnS (ZnS:Ni) nanocrystals as excellent visible-light-responsive photocatalysts for CO₂RR into formate. The wavelength-dependent quantum yield shows a significant contribution of Ni doping for visible light activity. A high selectivity (> 95%) of HCOOH production and remarkable quantum efficiency of 59.1% at 340 nm and 5.6% at 420 nm are obtained over ZnS:Ni (0.1%) colloidal nanocrystals modified by Cd²⁺. The proper balance between sulfur vacancies and extended visible light absorption of the constructed colloidal ZnS:Ni nanocrystals contributes to the prominent performance for CO₂RR. However, excessive doping of Ni does not guarantee an increase of photocatalytic CO₂RR due to a diminish of sulfur vacancies. The regulation of sulfur vacancies by Ni doping and their interplay on photocatalytic CO₂RR activity are presented and discussed. This work provides an in-depth insight of the role of dopant on vacancy modulation in photocatalyst beyond light absorption and a guidance for design of the potential photocatalyst for CO₂RR.

1. Introduction

Over the past few decades, the ever-increasing CO₂ atmospheric concentration and the diminishing reserves of the chemical feedstocks on earth have instigated scientists to seek for new alternatives for fuels [1–3]. To address the globally concerned problem, carbon sequestration was proposed as the long-term blueprint to impede the massive man-made CO₂ emissions [4–9]. Among the various methods of carbon mitigation, photocatalytic CO₂ reduction reaction (CO₂RR) has immense promise with the solar light as the sole input energy and hence serves as one of the most appealing and sustainable artificial photosynthetic approaches [10–15]. Despite enormous efforts and considerable achievements in solar-to-chemical conversion, the efficiency of

photocatalytic CO₂RR over semiconductors is still far from satisfactory.

With the two symmetric C=O bonds in a short line, CO₂ molecule is highly stable and peculiarly difficult to be activated [10,11,16]. Typically, a photocatalytic reaction is initiated by photogenerated charge pairs (e⁻ - h⁺). As for a CO₂RR, the photoexcited electrons are able to reach the surface from conduction band (CB), be captured by the adsorbed carbon species and participate in the photoredox reactions [17]. From a thermodynamic point of view, the CO₂RR requires a high CB position which only a handful semiconductors can satisfy. Zinc sulfide (ZnS) stands out with a CB minimum located at -1.04 V vs. NHE [18,19], indicating a thermodynamic feasibility for efficient CO₂RR. In addition, the fast carriers generation and transportation, non-toxicity and low-cost make it one of the most promising photocatalysts for

* Corresponding authors at: International Center for Materials Nanoarchitectonics (WPI-MANA), National Institute for Materials Science (NIMS), Namiki 1-1, Tsukuba, Ibaraki, 305-0044, Japan.

E-mail addresses: mengxg.materchem@163.com (X. Meng), jinhua.ye@nims.go.jp (J. Ye).

<https://doi.org/10.1016/j.apcatb.2018.12.010>

Received 6 October 2018; Received in revised form 29 November 2018; Accepted 3 December 2018

Available online 04 December 2018

0926-3373/ © 2018 Elsevier B.V. All rights reserved.

CO₂RR. Through constructing an all-inorganic reaction system comprised of the colloidal ZnS, we have achieved a breakthrough of photocatalytic CO₂ conversion into formate with 76% apparent quantum efficiency (280 nm) and 95% HCOOH selectivity [20]. Without any organic surface stabilization, the ZnS particles are quantized with an average diameter of ca. 3 nm. The shortened diffusion length within the ultra-small colloidal nanocrystals can slow down the recombination rates of photogenerated electrons and holes [21]. However, its intrinsic wide bandgap of about 3.7 eV determines it exclusively responsive to ultraviolet (UV) light which merely accounts for 4% solar spectrum [22]. It is necessitated to extend its light absorption to visible light region or longer wavelengths. Transition-metal dopants such as Bi, Fe, Pb, Cu, Ni, were reported capable of introducing an additional energy level within the band gap and narrowing the bandgap of ZnS [23,24]. Thus later, Cu was doped into the colloidal ZnS nanocrystals to narrow the bandgap and realize the visible light response [25].

Introducing anion vacancies has already been demonstrated as an effective avenue to boost the performance of oxide photocatalysts as the vacancies can activate the adsorbates and trap the photoexcited electrons to suppress the charge recombination, favorable for the catalytic reactions [26–39]. On account of the preparation method, it is envisaged that sulfur vacancies (S_v) intrinsically exist within the synthesized colloidal ZnS samples because S atoms are apt to escape in the form of H₂S in such aqueous system, which account for the active sites and exceptional performance. The role of elemental dopants is actually quite complicated beyond the light absorption. Previous work pointed out that Cu dopant changed to Cu⁺ and formed one sulfur vacancy adjacently [40]. But our theoretical calculation found the Ni dopant is not beneficial for the sulfur vacancy formation due to an increase of the formation energy.

Herein this work, Ni, as a noble-metal-free and non-toxic dopant, is selected to modify the electronic structure of ZnS. We constructed a colloidal system of Ni-doped ZnS (ZnS:Ni) nanocrystals in aqueous solution with loosely aggregated architecture furnishing with sufficient surface area and active sites. The synergy between doping and vacancy also attract us to look into the effect of Ni doping on S_v where rare reports set foot in, except the modulation of electronic structure. It is investigated and elucidated the correlation between the amount of foreign dopants and the CO₂RR performance. Some new perspectives into the CO₂RR photocatalyst underpinning the relationship between doping and vacancy are given.

2. Experimental

2.1. Catalyst preparation

Colloidal ZnS:Ni photocatalysts were fabricated by pouring the Na₂S solution (0.5 M) into equivalent volume of the mixture solution of ZnSO₄ (0.5 M) and a certain amount (0.1%, 0.2%, 0.5%, 1.0%, 2.0%, 4.0%) of NiSO₄ under vigorous stirring. After stirring overnight, the resulted suspensions were rinsed with water and centrifuged. The fresh precipitates were then dispersed in 100 ml ultrapure water (Direct-Q 3UV) for further photocatalytic activity evaluation.

2.2. Characterization

X-ray diffraction patterns (XRD) were obtained on an X-ray diffractometer (X'pert powder, PANalytical B.V., Netherlands) with Cu-K α radiation. The morphologies were observed on a Field-emission Scanning electron microscopy (FE-SEM, S-4800, Hitachi) and a Transmission electron microscopy (TEM, FEI Tecnai G2 F30) with a 300 kV accelerating voltage. The diffuse reflectance spectra (DRS) were measured on a Shimadzu UV-2500 spectrophotometer with an integrating sphere. The absorption spectra were transformed from the DRS spectra via Kubelka-Munk method. The Brunauer-Emmett-Teller (BET) surface area and CO₂ adsorption isotherms were obtained at 77 K

and room temperature, respectively, over BELsorp II mini (BEL Japan Inc.). The fluorescence (PL) spectra were measured by a fluorescence spectrometer (JASCO FP-6500) with the excitation wavelength of 280 nm over the colloidal ZnS:Ni suspensions of 1.0 g L⁻¹. X-ray photoelectron spectroscopy (XPS) (PHI Quantera SXM, ULVAC-PHI Inc., Japan) was used to analyse the compositions and valence states of the samples. Electron spin resonance (ESR) measurements were performed on JEOL JES-FA-200 at room temperature.

X-ray absorption fine structure (XAFS) spectra were measured at room temperature for Ni metal foil, ZnS:Ni (2.0%) samples in the transmission mode in the Photon Factory at KEK (Tsukuba) on beamline 9C. A Si (1 1 1) double-crystal monochromator and a pair of bent conical/cylinder mirrors and/or double flat mirrors were inserted into the X-ray beam path. The X-ray intensity was maintained at 67% of the maximum flux using a piezo-translator applied to the crystal to suppress higher harmonics. The slit in front of the I₀ ionization chamber had an opening size of 1 mm (vertical) \times 2 mm (horizontal). Ni K-edge spectra for NiS was measured in the transmission mode in the Photon Factory Advanced Ring at the High Energy Accelerator Research Organization on beamline NW10 A in which the storage ring energy was 6.5 GeV, and the ring current was 50 mA. A Si (3 1 1) double-crystal monochromator and a Pt-coated focusing cylindrical mirror were inserted into the X-ray beam path.

Spectra for the NiS (5.6 mg) sample diluted by boron nitride were measured at the beamline. The Ni K-edge absorption energy was calibrated to 8331.65 eV using the spectrum of a Ni metal foil (thickness 5 μ m). The obtained Ni K-edge XAFS data were analyzed using XDAP software package using modified Victoreen function, spline function, Fourier transform, and multiple-shell curve fitting.

2.3. Photocatalytic CO₂ reduction reaction

The photocatalytic CO₂ reductions over the aqueous colloidal ZnS:Ni nanocrystal suspensions were carried out in a Pyrex glass reaction cell with an upside quartz window linked to a gas-closed circulation system connected to a gas chromatography (GC) (GC-8 A, Shimadzu Co., Japan, Carrier gas: Ar) with a thermal conductivity detector (TCD) for online analysis of the H₂ production. 0.001 mol photocatalyst was suspended in 100 ml aqueous solution containing 0.5 M KHCO₃ and 0.5 M K₂SO₃ sacrificial reagents. For the formate production, 2.0 wt% CdSO₄ were added into the reaction solutions. Prior to the photo-reaction, the solution was evacuated until no O₂ and N₂ can be detected. The high-purity CO₂ (99.999%) was purged into the system for several times until the CO₂ adsorption was saturated. An AM 1.5 G solar simulator (WXS-80C-3 AM 1.5 G) and 300 W Xe lamp were used as the light source. The light intensity was measured on a spectroradiometer (Ushio Spectroradiometer, USR-40) for the measurement of apparent quantum efficiency.

2.4. Carbon-species products analysis

The CO and CH₄ evolved were sampled and analysed by GC (GC-14B, Shimadzu Co., Japan) equipped with a flame ionization detector (FID). The formate ions concentrations were determined by proton (¹H) spectra on a 400 MHz nuclear magnetic resonance (NMR) Spectrometer (ESC-400, JEOL, Japan) using 0.5 ml post-reaction solution supernatant mixed with 0.1 ml deuterated water (D₂O) and 0.05 μ L dimethyl sulfoxide (DMSO, Sigma, 99.99%). For isotope tracer measurement, ¹³CO₂ was purged in the system. To avoid the confusion of carbon source, the aqueous suspensions only contain 0.5 M K₂SO₃ sacrificial reagents apart from 0.001 mol photocatalyst and a certain amount of Cd²⁺ cocatalyst. The identification of ¹³CO was conducted on a gas chromatography-mass spectrometry (GC-MS, JMS-K9, JEOL Co., Japan). H¹³COOH was identified on the carbon (¹³C) spectrum on the NMR.

2.5. Electrochemical measurement

Photoelectrochemical measurements were conducted on a CHI electrochemical workstation ALS/CH model 650 A using a three-electrode system with 0.5 M Na_2SO_4 ($\text{pH} = 7$) electrolyte. For the preparation of working electrode, 1.0 ml of 2.5 mg mL^{-1} colloidal ZnS suspensions were mixed with 30 μL Nafion perfluorinated resin solution (Sigma-Aldrich) and sonicated. For the photocurrent measurement, the as-prepared suspensions were deposited on the indium tin oxide (ITO) substrates by spin coating. Platinum and Ag/AgCl (RE-1C; BAS Inc.) were employed as the counter electrode and reference electrode, respectively. An AM 1.5 solar simulator lamp was set as the light source with a light on/off cycle of 10 s. The flatband potential ($s(E_{\text{fb}})$) of the undoped and doped ZnS were obtained from Mott–Schottky plots at different frequencies (500, 1000, and 2000 Hz).

2.6. Theoretical calculations

The calculations of electronic structure were performed based on the plane-waved density functional theory calculations as implemented in a Vienna ab initio simulation package (VASP) code. The generalized gradient approximation (GGA) in a Perdew–Burke–Ernzerhof (PBE) functional were used for the exchange–correlation potential with a cutoff energy of 450 eV for the valence electrons. For the optical absorption calculations, the HSE06 hybrid functional was used to present the accurate band gap. Substitution of Zn atoms with Ni atom was conducted with a doping percentage of about 3.125%. The ZnS:Ni (110) surface is simulated using a 2×2 slab model consisting of five atomic layers of ZnS and a 16 Å vacuum region to avoid the interaction between two adjacent slabs. For the calculation of the density of states, $2 \times 2 \times 1$ Monkhorst k -point meshes were chosen to sample for the Brillouin-zone integrations of the slab model. All atoms are relaxed with the convergence tolerance set to 1×10^{-5} eV per atom and the residual force less than 0.02 eV/Å.

3. Results and discussion

3.1. Morphology and structure characterization

The colloidal ZnS:Ni photocatalysts with 0%, 0.1%, 0.2%, 0.5%, 1.0%, 2.0% and 4.0% doping amounts were directly synthesized by controlling the NiSO_4 precursor amount in an aqueous-phase co-

precipitation process. The morphologies are observed by transmission electron microscopy (TEM) (Fig. 1a) and scanning electron microscopy (SEM) (Fig. S1). Figs. 1a and S1 displays that the majority of particles in colloidal ZnS:Ni are easily agglomerated due to their extremely small dimensions and high surface energy. Despite the severe agglomeration under dehydrated conditions for TEM observation, several isolated nanocrystals are still distinguished as seen in Fig. 1b. The high-angle annular dark-field (HAADF) image and the energy-dispersive X-ray spectroscopy (EDX) elemental mappings under scanning transmission electron microscopy (STEM) mode exhibit a highly uniform distribution of Zn, S, Ni elements as shown in Fig. 1c–f, indicating Ni elements are homogeneously doped into the colloidal ZnS:Ni nanocrystals. Observation under the high-resolution TEM (HRTEM) found that the colloidal ZnS:Ni nanocrystals gradually crystallized under the electron beams and showed distinct lattice fringes. The interplanar spacing of the ZnS:Ni is 3.21 Å as marked in Fig. 1g, in accordance with the analytic result of the selected area electron diffraction (SAED) in Fig. 1h which shows the radius of the most distinguished diffraction ring is 0.310 nm, corresponding to (111) crystal plane of the cubic ZnS. Closer examination of the second and third diffraction rings are identified with interplanar spacing of 0.185 nm and 0.158 nm, well assigned to (220) and (311) crystal planes. This result is in well agreement with the three intensive peaks located at 28.6° , 47.8° , 56.6° indexed to 111, 220, 311 diffraction, respectively, in X-ray diffraction (XRD) pattern as present in Fig. 1i. The XRD pattern clearly showed the as-synthesized ZnS:Ni colloidal nanocrystals are indexed to a typical cubic sphalerite structure (JCPDS No. 77-2100) though the diffractogram is broad. There is no obvious deviation of the peak positions of the XRD patterns with the doping amount increasing from 0% to 4.0%, which might be attributed to the reason that the ionic radius of the four-coordinated Ni^{2+} (0.69 Å) is close to that of the Zn^{2+} (0.74 Å) [41]. No other discernable impurity peaks are detected, indicating Ni doping well retains the crystal structural phase of cubic ZnS nanocrystals in colloidal system.

According to the size distribution in high-resolution TEM (HR-TEM) images (Inset of Fig. 1b), the estimated average size of the colloidal ZnS:Ni nanocrystals is 3.5 ± 0.7 nm, in accord with the derived result from Scherrer's equation based on the X-ray powder diffraction (XRD) spectra, which give an average particle size of ca. 3 nm. When dispersing the samples in the liquid phase, the small dimensions can furnish with more surfaces and active sites for the photocatalytic CO_2RR which features as a surface reaction. This was testified through BET and volumetric CO_2 uptake measurement, which clarify the Ni doping effect

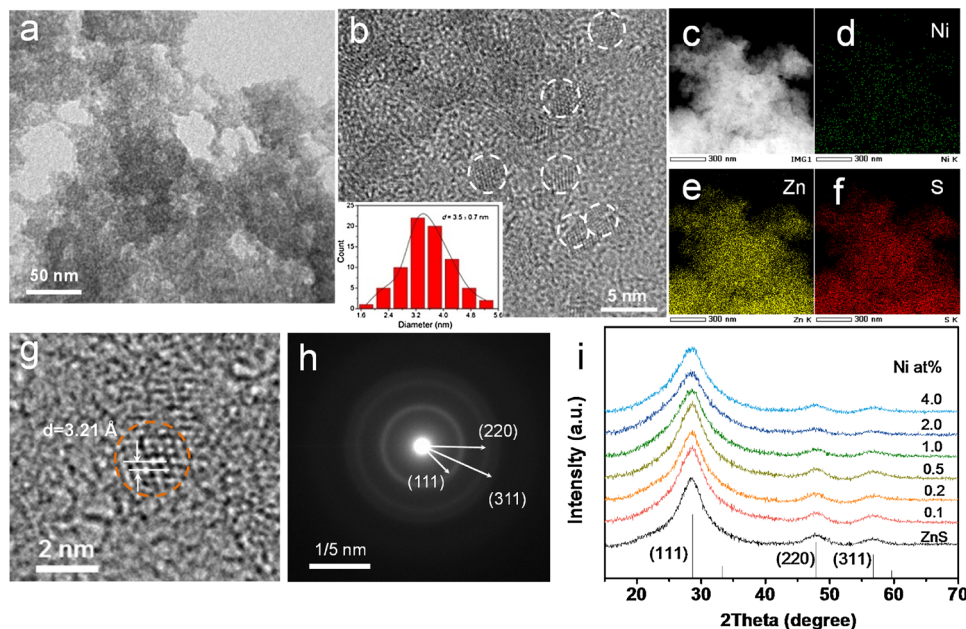


Fig. 1. Morphological and structural characterization. (a) Bright-field TEM image, (b) HRTEM image (Inset: size distribution), (c) HAADF-STEM image, (d–f) elemental mapping of Ni, Zn, S, (g) HRTEM image, (h) SAED pattern of the ZnS:Ni (2.0%) colloidal nanocrystals, (i) XRD pattern of the colloidal ZnS:Ni nanocrystals with doping amount from 0 to 4.0 %.

on the surface area and CO₂ adsorption capacity. To diminish the temperature effect on the structure of the low-crystalline nanocrystals, the colloidal ZnS and ZnS:Ni were dried by freeze-drying instead of heat treatment. As seen from Fig. S3a, the surface area of the ZnS:Ni (0.1%) is 192.19 m² g⁻¹, slightly larger than that of the ZnS:Ni (0.2%) (145.83 m² g⁻¹) and the undoped ZnS (133.30 m² g⁻¹) but nearly three times higher than that of the ZnS:Ni (2.0%) samples (60.40 m² g⁻¹). Although the dried structure can not fully reflect the liquid phase adsorption, it is supposed the smaller Ni doping will cause a disorder of the surface and slightly enlarge the surface area but decreased the adsorption sites with the doping amount increase. CO₂ uptake amount comparison in Fig. S3b also indicates the smaller amount of Ni (0.1%) and Ni (0.2%) doping maintained the CO₂ volumetric adsorption at higher level but the heavy doping amount like 2.0% will cause a slight decrease.

3.2. Electronic structure and photophysical properties

To gain insight into the electronic structure, we constructed the ZnS:Ni and perfect ZnS supercell slabs as schemed in Fig. S4 to implement the Density Functional Theory (DFT) calculations. The theoretically calculated band structure and projected density of states (PDOS) are displayed in Fig. 2. Ni dopant introduced an occupied state above the valence band of the pristine ZnS with an additional contribution from S orbitals. The created new energy level within the band gap extend the absorption to visible light range as the simulated optical absorbance spectrum predicts in Fig. S5. The UV – vis absorption spectra (Fig. 3) of the ZnS:Ni colloidal crystallites transformed from the diffuse reflectance spectra (DRS) via K-M method possess an intrinsic absorption feature edged at 340 nm and enhanced photo-absorption in the visible light ranging from 340 ~ 470 nm, related to the transition from

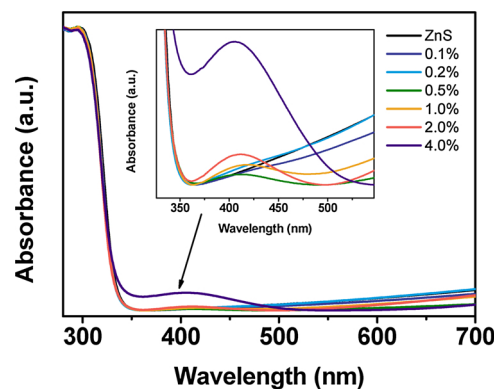


Fig. 3. UV-vis absorption spectra of ZnS:Ni colloidal nanocrystals.

the occupied Ni 3d orbitals to the hybridization of Zn 4s-S 3p orbitals. The accordance of UV – vis absorption spectra with the simulated optical absorption configuration derived from the electron structure, also testifies Ni is successfully doped into ZnS crystal lattice. We can also observe from the optical photographs in Fig. S6, the colour of the as-synthesized Ni-ZnS colloidal varied from bright yellow to deep yellow as with the doping amount increment from 0.1% to 4.0%. Herein we have conducted Mott-Schottky measurement and XPS valence band (VB) to roughly estimate the conduction band and valence band edges as seen in Fig. S7 (The calculation method can be found in Supporting Information). It is clear to see the Ni dopant created a new level at a position of 0.8 eV above the VBM of ZnS, well correlated with what the theoretical simulation predicts. It is worth mentioning that the longer wavelength absorption tails in the visible region is ascribed to S_v [42], attributed to the transition from a newly created midgap state by

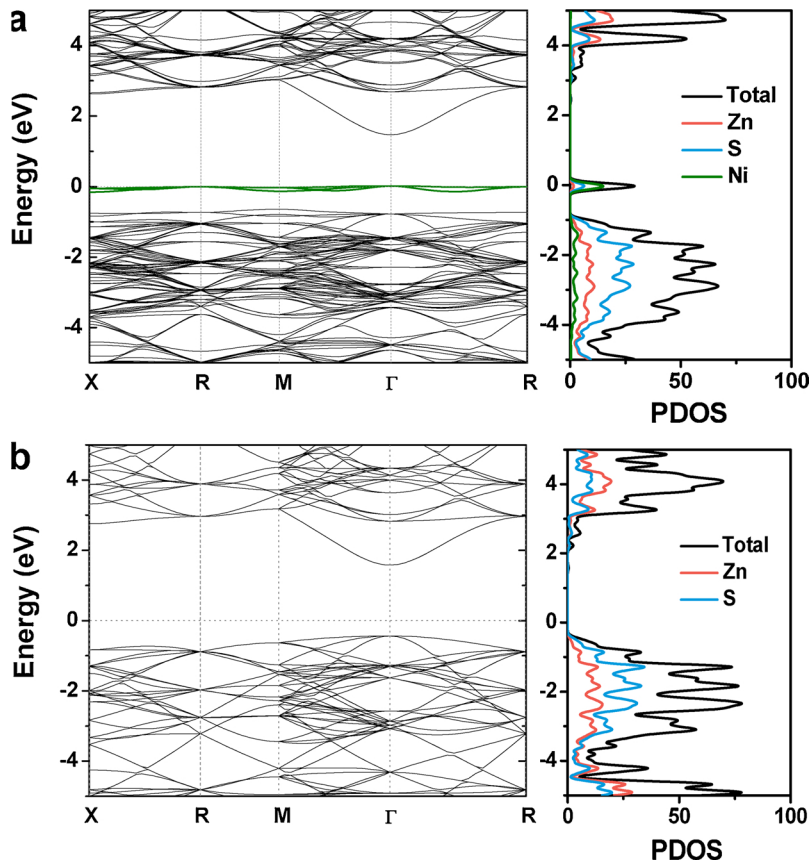


Fig. 2. The electronic band structure and the decomposition of the total density of states (DOS) into partial DOS of Ni, Zn and S orbitals of (a) ZnS:Ni (2.7%) and (b) undoped ZnS, respectively.

S_v just below CB to the CB of ZnS, suggesting the abundant S_v within the as-prepared samples. In addition, the tails level off with an increase of the doping amount until the 4.0% Ni-doped sample, indicating the Ni doping can modulate the amount of sulfur vacancies within the doped ZnS colloidal nanocrystals.

3.3. Photocatalytic CO₂RR activity

The CO₂RR of the ZnS:Ni colloidal suspension was assessed over the CO₂-saturated KHCO₃ solvent with K₂SO₃ as the electron donors in the pyrex cell with a quartz lid. The experimental setup can be found in the Fig. S8. A 300 W full arc Xe lamp with and without cutoff filter (> 420 nm) were first adopted as the outer irradiation source. As reported previously, Cd²⁺ can serve as an efficient cocatalyst for the highly selective formate production [20,25]. Herein 2.0% Cd²⁺ was added to promote the formate production. When the photocatalytic reaction was carried out, photogenerated holes were irreversibly consumed by the reducing reagent SO₃²⁻ and thereby boosting the photogenerated electrons in the conduction band transfer to chemisorbed CO₂ for the reduction. The evolved rates of H₂, CO and the liquid product, HCOOH under irradiance with wavelength > 420 nm are figured in Fig. 4; H₂, CO and HCOOH were produced at a rate as high as 23.8 $\mu\text{mol h}^{-1}$, 0.18 $\mu\text{mol h}^{-1}$ and 427.5 $\mu\text{mol h}^{-1}$, respectively, when full arc Xenon lamp was employed. As contrast, the undoped ZnS has no activity under the visible light irradiation. Then to simulate the photocatalytic CO₂ reduction under solar light, the reaction was carried out under an AM 1.5 G solar simulator. The time-conversion plot of the gaseous products, H₂ and CO over time course and the average production rate of formate are figured in Fig. 5a–c. Even under the weak sunlight, the formate production can reach up to 137.9 $\mu\text{mol h}^{-1}$ with a selectivity up to 99% over ZnS:Ni (0.1%) (Fig. 5c). The apparent quantum efficiency (AQY) curve in Fig. 5d clearly shows a wavelength-dependence tracking the absorption of the ZnS:Ni. In this experiment, the AQY is 59.1% @ 339.3 nm and 5.6% @ 417.9 nm, dominated by the intrinsic ultraviolet absorption and the Ni doping-induced visible light absorption, respectively. In addition, despite a negligible absorption induced by Ni doping at 480 nm, there is an obvious AQY at 480.4 nm with a value of 1.19%, suggesting the abundant S_v also contributes to the visible-light-responsive activity over the ZnS:Ni.

The CO₂RR activity over the series of ZnS:Ni were also tested under different light source as shown in Figs. S10–12 with a different optimal doping amount of Ni. It can be found the optimal doping amount of Ni shifts to larger when increasing the visible light component in the irradiation source, demonstrating the Ni doping effect and existence of S_v successfully extends the CO₂RR activity of colloidal ZnS nanocrystals into visible light region and enhances the formate production under

solar light.

The isotope experiment using ¹³CO₂ under the identical reactant conditions excluding the utilization of KHCO₃ was carried out to validate the source of the produced CO and HCOOH. The GC–MS results in Fig. S13 clearly demonstrate the production of ¹³CO ($m/z = 29$). The identification of liquid H¹³COO⁻ was performed by ¹³C nuclear magnetic resonance (NMR) spectra. The peaks at $\delta = 170.5$ ppm and 160.5 ppm assigned to H¹³COO⁻ and H¹³CO₃⁻ in ¹³C NMR spectrum (Fig. S14) and the doublet peak at 8.1 and 8.6 ppm in ¹H NMR spectrum (Fig. S15) together confirm the liquid product HCOOH all comes from the ¹³CO₂.

To test the ZnS:Ni photocatalysts' durability, long-term photochemical CO₂ reduction experiments were performed over 80 h. As displayed in the Fig. S16, no obvious deactivation was observed in this long period, underlying the colloidal ZnS:Ni exhibits quite strong durability. Notably, even the CO production rate were slightly higher in the late stage as shown.

3.4. The correlation between Ni dopant and sulfur vacancy

It has been already stated the abundant sulfur vacancies in such aqueous colloidal structure induce the excellent performance for CO₂RR and Ni doping increase the valence band position with regard to the band structure, improving the visible light utilization and hence the activity under solar light. But the fact that light doping increased the activity nearly three times and heavier doping of Ni leading to a decrease of CO₂RR production raise a question why the optimal activity is obtained at 0.1% doping amount. We measured the photocurrents (in Fig. S17) of the representative samples to describe the charge separation efficiency and carrier transport under irradiation but found that only slight discrepancies were presented, not sufficient to account for the large difference in activity. Then we turned to the adsorption sites indicated by the BET and CO₂ uptake experiment for the reason. Our theoretical calculation predicts the sulfur vacancy formation energy increases 0.76 eV after incorporation of Ni, indicating the Ni doping is not beneficial for the formation of the S_v .

The factors of Ni dopants and S_v are actually complex and inter-related. To get a deeper insight into how the Ni doping affects the S_v and photocatalytic CO₂RR performance, the electron spin resonance (ESR) spectroscopy was further employed to observe the electron performance as shown in Fig. 6a. It was clearly noted that a sharp signal at $g_1 = 1.999 \pm 0.004$ and a broad signal located at $g_2 = 2.007 \pm 0.004$ were detected both over the undoped and ZnS:Ni colloidal nanocrystals. According to the reference, the broad signal is the feature of the dipolar interaction between the physically adsorbed molecular oxygen on the paramagnetic centers as we performed the ESR in air [43]; the sharp signal can be assigned to the F center, a singly negatively charged S_v in the cubic ZnS crystals, strongly supporting the existence of S_v [44]. No Ni-related signatures were observed in this range [45]. As the ESR signal is correlated with the density of paramagnetic electrons from S_v , it was found the smaller Ni doping (< 0.2%) results in a higher level of surface active sites according to the larger intensity of the chemisorbed oxygen signals but the doping amount more than 0.2% will dramatically decrease the S_v within the nanocrystals, consistent with the surface area and absorption observations stated above.

Photoluminescence (PL) spectroscopy is another efficient and direct way to figure out the photogenerated charge carriers dynamics under a certain excitation wavelength. From the PL emission spectra in Fig. 6b, we can have a clear view of the energy states within the bandgap. Under 280 nm excitation, there are two major emission peaks. The 320 nm emission peak (green area) is assigned to the intrinsic transition of photoelectrons and holes from conduction band to valence band. With the new states above the valence band maximum (VBM) created by Ni to trap the holes and promote the charge separation, the reduced intensity at 320 nm with the increasing Ni amount is easy to correlated with the suppressed recombination. The broad peak centered at 425 nm

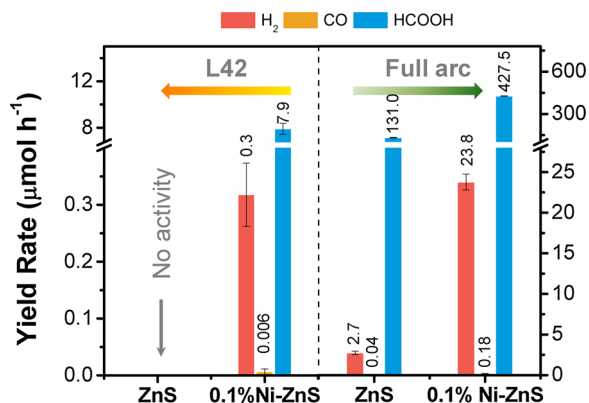


Fig. 4. Evolution rates of H₂, CO and HCOOH under 300 W full arc Xenon lamp with a cutoff filter of 420 nm (left panel) and without any cutoff filter (right panel) over colloidal ZnS:Ni (0.1%) nanocrystals.

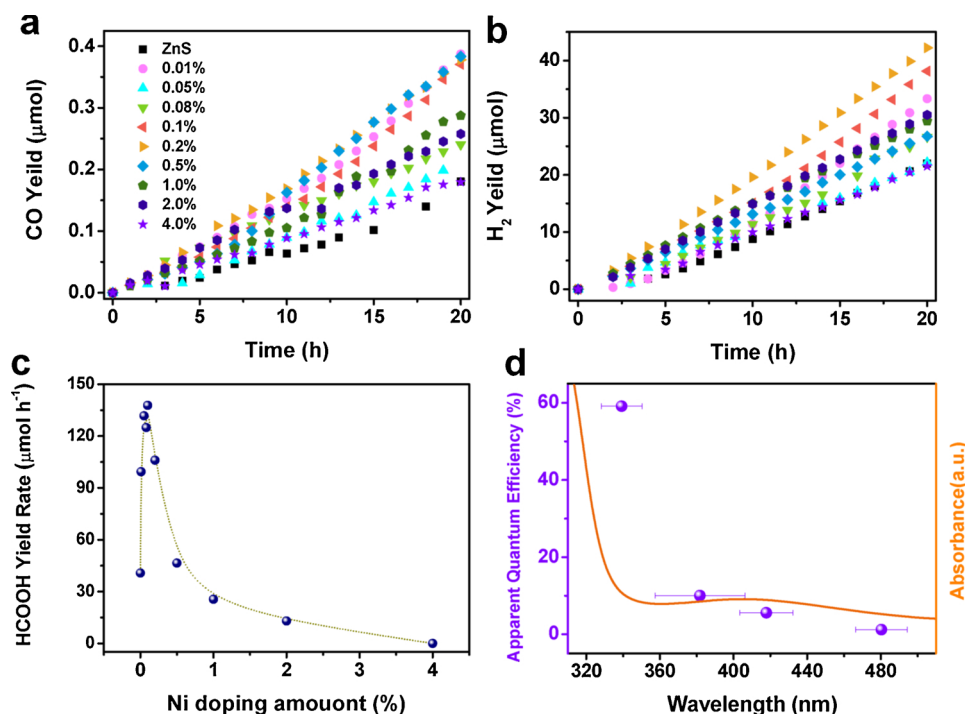


Fig. 5. Time-conversion plot of the gaseous product under AM 1.5 simulator: (a) CO and (b) H_2 . (c) HCOOH production rate of colloidal ZnS:Ni with different doping amount of Ni (d) The wavelength-dependent AQY of photocatalytic HCOOH production over colloidal ZnS:Ni (0.1%) nanocrystals.

peak (yellow area) arising from the deep trap level near conduction band was reported from S_v in the previous literature [46,47]. From the decreasing intensities of the blue emission at 425 nm, it is deduced Ni doping can curtail the excessive S_v in the undoped ZnS, in well accord with what we have observed in ESR spectra.

Further chemical states analysis of the colloidal ZnS:Ni nanocrystals are conducted on X-ray photoelectron spectroscopy (XPS). The XPS

survey spectrum is presented in Fig. S18. The pristine ZnS, ZnS:Ni (0.1%), ZnS:Ni (0.2%) and ZnS:Ni (4.0%) are selected as the representative samples of the undoped, optimal doped, light doped and heavier doped one. As shown in Fig. 6c, the high-resolution XPS spectrum of Zn 2p reveals that there is a pair of peaks located at 1022.4 eV and 1045.4 eV binding energy, which are assigned to Zn $2p_{3/2}$ and Zn $2p_{1/2}$ of undoped ZnS colloidal nanocrystals. When Ni was doped in the

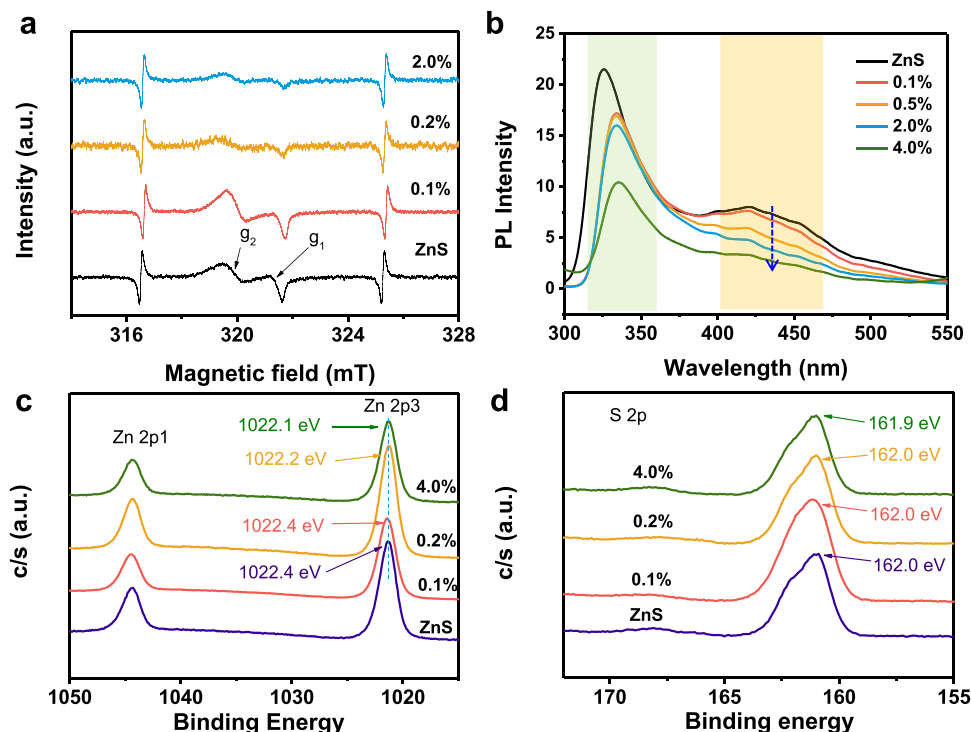


Fig. 6. (a) ESR spectra and (b) PL spectra of undoped ZnS and ZnS:Ni nanocrystals at room temperature. The 425 nm emission represents the sulfur vacancy signature. High-resolution XPS spectra of (c) Zn 2p and (d) S 2p, respectively of the undoped, ZnS:Ni (0.1%), ZnS:Ni (0.2%) and ZnS:Ni (4.0%) nanocrystals.

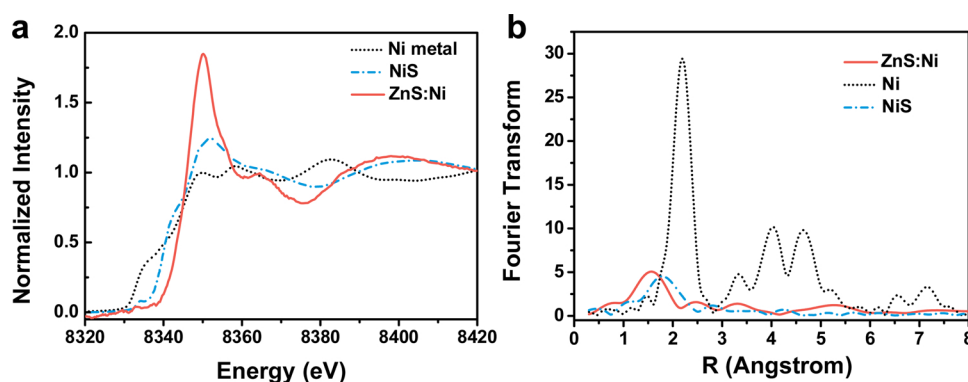


Fig. 7. Ni K-edge XANES (a) and Fourier transform of EXAFS spectra (b) for Ni metal foil (thickness 5 μm , black line), NiS (5.6 mg, blue line) and fresh ZnS:Ni (2.0%) (50 mg, red line). The XRD pattern of the as-prepared NiS is shown in Fig. S21. k^3 -weighted EXAFS oscillation with best-fit results in k -space and R -space for first-shell (Ni-S) of ZnS:Ni is seen in Fig. S22. (For interpretation of the references to colour in this figure legend, the reader is referred to the web version of this article).

ZnS at 0.1%, the binding energy of the Zn 2p peaks and S 2p peak maintained their original position, suggesting the small doping will not obviously affect the oxidation states of the elements. But the major Zn 2p_{3/2} peak shifts to 1022.2 eV and to 1022.1 eV for ZnS:Ni (0.2%) and ZnS:Ni (4.0%), equivalent to a negative shift of ~ 0.2 eV and ~ 0.3 eV with respect to the undoped counterpart, respectively. It is reasonable to deduce that Ni doping leads to a decrease of the electron density of the positively charged Zn ion adjacent to the S_v and hence a lower binding energy. From Fig. 6d, we can observe the S 2p peaks slightly shifts from 162.0 eV toward lower binding energy of 162.0 eV and 161.9 eV for ZnS:Ni (0.2%) and ZnS:Ni (4.0%), respectively. The lowering of S 2p binding energy also demonstrates the weakened Zn-S bonds near the dopant site caused by Ni-S bond formation.

As XPS measurement failed to show any signal of Ni because the photoelectron energy was not enough to penetrate the nanocrystal even though we adjusted the doping amount to 4.0% (Fig. S19) and Raman spectra could not show obvious difference, either (Fig. S20), the synchrotron-based XAFS was collected over ZnS:Ni (2.0%) to establish the oxidation state and local structure of the Ni dopant.

In the normalized Ni K-edge X-ray absorption near edge structure (XANES) (Fig. 7a), the structure of ZnS:Ni differs from that of the Ni foil and NiS reference, excluding the existence of Ni aggregation or the formation of NiS. The white line position of the absorption edge at 8350.1 eV, well correlated with that of the NiO and NiS, indicates Ni²⁺ dominates as the oxidation state. When k range was extended up to 8.2 \AA^{-1} and the k^3 -weighted EXAFS oscillation was fitted in a k space and R space (Fig. S22), the best fit of the scattering interaction can be obtained with a one-shell fit of Ni-S in the EXAFS spectrum (Fig. 7b). The derived coordination number of the Zn-S shell is 3.96, reflecting the local coordination of Ni is tetra-coordinated by four sulfur atoms. As the Zn-S distance (2.34 \AA) is slightly shorter than the Ni-S bond length (2.47 \AA) [48], the smaller magnitude in the transform of ZnS:Ni than NiS suggests a contraction and disorder of the lattice when Ni is doped. Overall, the edge data and EXAFS data confirm the dominant Ni²⁺ status and the bonding coordination in the as-prepared ZnS:Ni. However, careful observation in the pre-edge area (See Fig. S23) and main peak found a slight shift towards lower energy with respect to the NiS, indicating an increased charge density of Ni. The Bader charge calculation further demonstrate the electronic configuration of Ni with 10.00 valence electrons changes to 9.12 valence electrons in the ZnS:Ni with part of 3d⁹, $s = 1/2$ configuration. The rest of two electrons after one sulfur atoms escape are easily trapped by the Ni dopant if the doping amount is excessive. This might be the reason why sulfur vacancies could be reduced by Ni dopant.

From the discussion above, large amount of sulfur vacancies in the bulk within the pristine undoped ZnS nanocrystals will bring about the severe recombination of charge carriers and suppress the reduction activity. As Ni doping are apt to localize the electrons on sulfur vacancies and reduce the S_v , light doping can regulate the S_v to the optimal abundance and induce a significant enhancement in activity;

heavier doping leads to a great loss of S_v and a low performance adversely despite an extended light absorption in visible region.

4. Conclusion

Solar-driven CO₂ reduction was successfully realized over ZnS:Ni colloidal nanocrystals with an optimal doping amount of 0.1%. Loading with Cd²⁺, the HCOOH production over ZnS:Ni colloidal nanocrystals has reached up to 427 $\mu\text{mol}\cdot\text{h}^{-1}$ under 300 W Xe lamp and 138 $\mu\text{mol}\cdot\text{h}^{-1}$ (selectivity $\sim 99\%$) under 1 sun. The AQY at 340 nm in the UV region and at 420 nm in the visible light region are 59.1% and 5.6%, respectively, at the front ranks in the currently reported photocatalytic CO₂RR systems. The reason why photoconversion of CO₂ is optimized at a small doping amount (0.1%) of Ni is explained as a proper balance between the increased light absorption and decreased S_v . Demonstrated by PL, ESR and XPS, it was found the Ni dopants can modulate the S_v amount in the loose-structured ZnS:Ni colloidal architecture. Light doping of Ni will maintain the abundant S_v , suppressing the charge recombination in the bulk; heavier doping of Ni will cause the diminishing of S_v , unfavorable for the CO₂RR. Thus, only appropriate doping amount can give rise to the optimal performance of the photocatalytic CO₂RR. The discovery offers a unique insight into the doping strategy and modulation of anion vacancies on the photocatalysts towards CO₂ reduction.

Conflict of interest

The authors declare no conflict of interest.

Acknowledgements

The work received the financial support from the World Premier International Research Center Initiative (WPI Initiative) on Materials Nanoarchitectonics (MANA), MEXT, Japan, the National Basic Research Program of China (973 Program, 2014CB239301), the National Natural Science Foundation of China (21633004 and 21703065) and JSPS KAKENHI Grant Number JP18H02065. X-ray absorption experiments were conducted under the approval of the Photon Factory Proposal Review Committee (2016G577).

Appendix A. Supplementary data

Supplementary material related to this article can be found, in the online version, at doi:<https://doi.org/10.1016/j.apcatb.2018.12.010>.

References

- [1] J.L. White, M.F. Baruch, J.E. Pander Iii, Y. Hu, I.C. Fortmeyer, J.E. Park, T. Zhang, K. Liao, J. Gu, Y. Yan, T.W. Shaw, E. Abelev, A.B. Bocarsly, Chem. Rev. 115 (2015) 12888–12935.
- [2] T.J. LaTempa, S. Rani, N. Bao, C.A. Grimes, Nanoscale 4 (2012) 2245.

- [3] S. Wang, X. Wang, *Appl. Catal. B: Environ.* 162 (2015) 494–500.
- [4] G.A. Olah, G.K.S. Prakash, A. Goepfert, *J. Am. Chem. Soc.* 133 (2011) 12881–12898.
- [5] J.J. Concepcion, R.L. House, J.M. Papanikolas, T.J. Meyer, *Proc. Natl. Acad. Sci.* 109 (2012) 15560–15564.
- [6] G. Zhao, W. Zhou, Y. Sun, X. Wang, H. Liu, X. Meng, K. Chang, J. Ye, *Appl. Catal. B: Environ.* 226 (2018) 252–257.
- [7] G. Zhao, H. Pang, G. Liu, P. Li, H. Liu, H. Zhang, L. Shi, J. Ye, *Appl. Catal. B: Environ.* 200 (2017) 141–149.
- [8] G. Chen, R. Gao, Y. Zhao, Z. Li, G.I.N. Waterhouse, R. Shi, J. Zhao, M. Zhang, L. Shang, G. Sheng, X. Zhang, X. Wen, L.Z. Wu, C.H. Tung, T. Zhang, *Adv. Mater.* 30 (2018).
- [9] Y. Hao, A. Steinfeld, *Sci. Bull.* 62 (2017) 1099–1101.
- [10] H. Pang, T. Masuda, J. Ye, *Chem. Asian J.* 13 (2018) 127–142.
- [11] X. Chang, T. Wang, J. Gong, *Energy Environ. Sci.* 9 (2016) 2177–2196.
- [12] J. Qin, S. Wang, X. Wang, *Appl. Catal. B: Environ.* 209 (2017) 476–482.
- [13] Y. Su, Z. Zhang, H. Liu, Y. Wang, *Appl. Catal. B: Environ.* 200 (2017) 448–457.
- [14] Z. Sun, J.M.T.A. Fischer, Q. Li, J. Hu, Q. Tang, H. Wang, Z. Wu, M. Hankel, D.J. Searles, L. Wang, *Appl. Catal. B: Environ.* 216 (2017) 146–155.
- [15] R. Shi, G.I.N. Waterhouse, T. Zhang, *Solar RRL* 1 (2017) 1700126.
- [16] S. Xie, Q. Zhang, G. Liu, Y. Wang, *Chem. Commun.* 52 (2016) 35–59.
- [17] H. Tong, S. Ouyang, Y. Bi, N. Umezawa, M. Oshikiri, J. Ye, *Adv. Mater.* 24 (2012) 229–251.
- [18] R. Zhou, M.I. Guzman, *J. Phys. Chem. C* 118 (2014) 11649–11656.
- [19] X. Hao, Y. Wang, J. Zhou, Z. Cui, Y. Wang, Z. Zou, *Appl. Catal. B: Environ.* 221 (2018) 302–311.
- [20] X. Meng, Q. Yu, G. Liu, L. Shi, G. Zhao, H. Liu, P. Li, K. Chang, T. Kako, J. Ye, *Nano Energy* 34 (2017) 524–532.
- [21] M. Kanemoto, T. Shiragami, C. Pac, S. Yanagida, *J. Phys. Chem.* 96 (1992) 3521–3526.
- [22] H. Pang, G. Zhao, G. Liu, H. Zhang, X. Hai, S. Wang, H. Song, J. Ye, *Small* 14 (2018) e1800104.
- [23] A. Kudo, Y. Miseki, *Chem. Soc. Rev.* 38 (2009) 253–278.
- [24] G. Yang, D. Chen, H. Ding, J. Feng, J.Z. Zhang, Y. Zhu, S. Hamid, D.W. Bahnemann, *Appl. Catal. B: Environ.* 219 (2017) 611–618.
- [25] X. Meng, G. Zuo, P. Zong, H. Pang, J. Ren, X. Zeng, S. Liu, Y. Shen, W. Zhou, J. Ye, *Appl. Catal. B: Environ.* 237 (2018) 68–73.
- [26] Y. Ji, Y. Luo, *J. Am. Chem. Soc.* 138 (2016) 15896–15902.
- [27] S. Gao, B. Gu, X. Jiao, Y. Sun, X. Zu, F. Yang, W. Zhu, C. Wang, Z. Feng, B. Ye, Y. Xie, *J. Am. Chem. Soc.* 139 (2017) 3438–3445.
- [28] X. Jiao, Z. Chen, X. Li, Y. Sun, S. Gao, W. Yan, C. Wang, Q. Zhang, Y. Lin, Y. Luo, Y. Xie, *J. Am. Chem. Soc.* 139 (2017) 7586–7594.
- [29] S. Gao, Y. Lin, X. Jiao, Y. Sun, Q. Luo, W. Zhang, D. Li, J. Yang, Y. Xie, *Nature* 529 (2016) 68–71.
- [30] W. Tu, Y. Xu, J. Wang, B. Zhang, T. Zhou, S. Yin, S. Wu, C. Li, Y. Huang, Y. Zhou, Z. Zou, J. Robertson, M. Kraft, R. Xu, *ACS Sustain. Chem. Eng.* 5 (2017) 7260–7268.
- [31] B. Wang, X. Wang, L. Lu, C. Zhou, Z. Xin, J. Wang, X.-k. Ke, G. Sheng, S. Yan, Z. Zou, *ACS Catal.* 8 (2017) 516–525.
- [32] Z. Geng, X. Kong, W. Chen, H. Su, Y. Liu, F. Cai, G. Wang, J. Zeng, *Angew. Chem. Int. Ed.* 57 (2018) 6054–6059.
- [33] C. Li, T. Wang, Z.J. Zhao, W. Yang, J.F. Li, A. Li, Z. Yang, G.A. Ozin, J. Gong, *Angew. Chem. Int. Ed.* 57 (2018) 5278–5282.
- [34] X. Chen, L. Liu, P.Y. Yu, S.S. Mao, *Science* 331 (2011) 746.
- [35] M. Wang, L. Cai, Y. Wang, F. Zhou, K. Xu, X. Tao, Y. Chai, *J. Am. Chem. Soc.* 139 (2017) 4144–4151.
- [36] G. Li, G.R. Blake, T.T. Palstra, *Chem. Soc. Rev.* 46 (2017) 1693–1706.
- [37] F. Wang, S. He, H. Chen, B. Wang, L. Zheng, M. Wei, D.G. Evans, X. Duan, *J. Am. Chem. Soc.* 138 (2016) 6298–6305.
- [38] Y. Zhao, G. Chen, T. Bian, C. Zhou, G.I. Waterhouse, L.Z. Wu, C.H. Tung, L.J. Smith, D. O'Hare, T. Zhang, *Adv. Mater.* 27 (2015) 7824–7831.
- [39] Y. Zhao, Y. Zhao, G.I.N. Waterhouse, L. Zheng, X. Cao, F. Teng, L.Z. Wu, C.H. Tung, D. O'Hare, T. Zhang, *Adv. Mater.* 29 (2017).
- [40] Z. Mei, B. Zhang, J. Zheng, S. Yuan, Z. Zhuo, X. Meng, Z. Chen, K. Amine, W. Yang, L.W. Wang, W. Wang, S. Wang, Q. Gong, J. Li, F.S. Liu, F. Pan, *Nano Energy* 26 (2016) 405–416.
- [41] G. Murugadoss, *J. Lumin.* 132 (2012) 2043–2048.
- [42] G. Wang, B. Huang, Z. Li, Z. Lou, Z. Wang, Y. Dai, M.H. Whangbo, *Sci. Rep.* 5 (2015) 8544.
- [43] A. Tetsuya, M. Teruyoshi, S. Koichi, *Japn. J. Appl. Phys.* 8 (1969) 1411.
- [44] Z. Fang, S. Weng, X. Ye, W. Feng, Z. Zheng, M. Lu, S. Lin, X. Fu, P. Liu, *ACS Appl. Mater. Interfaces* 7 (2015) 13915–13924.
- [45] M. Surma, A. Zakrzewski, M. Godlewski, T. Surkova, *Acta Phys. Pol. A* 1 (1995) 221–224.
- [46] H. Tang, G. Xu, L. Weng, L. Pan, L. Wang, *Acta Mater.* 52 (2004) 1489–1494.
- [47] N.D.P.H. Borse, R.F. Shinde, S.K. Date, S.K. Kulkarni, *J. Mater. Sci.* (1999) 6087–6093.
- [48] H. Hosokawa, K. Murakoshi, Y. Wada, S. Yanagida, M. Satoh, *Langmuir* 12 (1996) 3598–3603.